Journal of Advanced Ceramics
2023, **12**(4): 848–860
https://doi.org/10.26599/JAC.2023.9220725
ISSN 2226-4108
CN 10-1154/TQ

Research Article

Thermometric properties of $Na_2Y_2TeB_2O_{10}:Tb^{3+}$ green phosphor based on fluorescence/excitation intensity ratio

Yuefei Xiang†, Lin Yang†, Canyuan Liao, Xianfeng Xiang, Xiangkai Tang, Hanlin Tang, Jing Zhu*

Key Laboratory of LCR Materials and Devices of Yunnan Province, *Yunnan Key Laboratory of Carbon Neutrality and Green Low-carbon Technologies*, *School of Materials and Energy*, *Yunnan University*, *Kunming 650091*, *China*

Received: October 27, 2022; Revised: January 12, 2023; Accepted: January 27, 2023

Abstract: For noncontact optical thermometry, in contrast with fluorescence intensity ratio (FIR) technology, excitation intensity ratio (EIR) technology has been seriously limited due to low sensitivity. Moreover, by exploring all possible temperature-dependent response, developing multimode optical thermometry is of great importance. In this work, a new $Na_2Y_2TeB_2O_{10}$ (NYTB):Tb^{3+} phosphor is obtained by a solid-state reaction. Based on FIR and EIR models of Tb^{3+}, thermometric properties are studied thoroughly. Excellent relative and absolute sensitivity (S_R and S_A) are acquired due to the significant difference in emission/excitation lines in response to temperature. Meanwhile, Tb^{3+} content-dependent luminescence quenching mechanism is discussed. This study shows a feasible route for exploiting well-performing FIR-/EIR-based thermometric materials.

Keywords: $Na_2Y_2TeB_2O_{10}$ (NYTB); Tb^{3+} ion; photoluminescence (PL); thermometric properties

1 Introduction

Temperature is a vital parameter in industrial and civil areas, which makes developing temperature-detecting technology significant [1–3]. The shortcomings of conventional contact thermometers include environmental restrictions and long response time, which gradually cannot meet the actual usage requirements [4–6]. Hereby, Ghahrizjani *et al*. [7] and Cheng *et al*. [8] have paid much research to noncontact temperature-detecting technologies. Among these technologies, the optical thermometry method based on temperature-dependent luminescent properties of a phosphor is a fascinating issue owing to the advantages of noncontact model, high resolution, and fast response [8,9].

For optical temperature measurements, diverse strategies have been developed such as fluorescence intensity ratio (FIR), excitation intensity ratio (EIR), fluorescence lifetime, and emission intensity/position/bandwidth [10–14]. The mechanism of the FIR/EIR for optical thermometry focuses on studying the relationship between the FIR/EIR and the temperature [15]. The FIR approach can be achieved by monitoring the difference between the two emission peaks in response to the temperature. For instance, a fluorescence thermometer has been extensively investigated based on thermally-coupled energy levels of Er^{3+}, Pr^{3+}, and Nd^{3+} [16–18]. Recently, an EIR model has been increasingly

† Yuefei Xiang and Lin Yang contributed equally to this work.

* Corresponding author.
E-mail: jzhu@ynu.edu.cn

developed [10]. Compared with an FIR model, the EIR model provides more information about exciting levels of luminescence centers that cannot be detected in a emission spectrum [19]. The EIR model provides an efficient method for constructing a new high-performance thermometer.

Among rare-earth ions, the $^5D_4\rightarrow(^7F_6$, $^7F_5$, $^7F_4$, and $^7F_3)$ emissions of Tb^{3+} ions present opposite temperature-dependent behaviors, which are suitable for FIR thermometry with high relative sensitivity (S_R). Besides, $^5D_3$ and $^5D_4$ ground levels of Tb^{3+} can be used to realize the EIR thermometry due to the strong temperature-sensitive difference. This arouses our interest in developing multimode optical thermometry in Tb^{3+}-activated phosphors. Recently, low-lying thermally-coupled $^7F_5$ and $^7F_6$ principle of Tb^{3+} was employed to investigate temperature sensing performances of glass–ceramic materials of Ba_2LaF_7:Tb^{3+} [20] and Na_2GdF_7:Tb^{3+} [21], which presented the maximum S_R ($S_{R\text{-}max}$) of 2.88 %·K^{-1} at 300 K and 2.33 %·K^{-1} at 310 K. Drabik *et al*. [22,23] developed a single-band-ratiometric method to utilize opposite thermal dependence of a characteristic emission for Tb^{3+} excited by the two different wavelengths (λ). For example, based on the opposite temperature-dependent behaviors of the $^5D_4\rightarrow{}^7F_3$ emission under the excitations of the $^7F_6\rightarrow{}^5D_4$ and $^7F_5\rightarrow{}^5D_4$ transitions, it is reported that $KLaP_4O_{12}$:0.1Tb^{3+} exhibited the $S_{R\text{-}max}$ value of 5.5 %·K^{-1} [23]. Wei *et al*. [24] researched the thermometric properties of $CaNb_2O_6$:Tb^{3+} in terms of the descending difference of temperature-dependent emissions from a host and a Tb^{3+} activator. The thermometric strategy associated with the host was also reported in $Sr_8MgCe(PO_4)_7$:Tb^{3+} [25], Y_2O_3:Tb^{3+} [26], and Lu_2O_3:Tb^{3+} [26] phosphors. Especially, Li *et al*. [27] reported the EIR in La_2ZnTiO_6:Tb^{3+}. According to the different thermal dependence of 381 nm (4f–4f of Tb^{3+}), 285 nm (4f–5d of Tb^{3+}), and 313 nm (intervalence charge transfer) excitation bands, the EIR models (EIR(I_{381}/I_{285}) and EIR(I_{381}/I_{313})) were established to obtain the maximum absolute sensitivity ($S_{A\text{-}max}$) (4.46×10^{-2} K^{-1}) and S_R (0.727 %·K^{-1}). To our knowledge, there are no reports for Tb^{3+}-activated phosphors with FIR-/EIR-based thermometric properties.

Considering our early work on the yellow $Na_2Y_2TeB_2O_{10}$ (NYTB)-based phosphor activated with a Dy^{3+} ion [28], we prepared a Tb^{3+}-activated NYTB phosphor via a solid-state reaction in this work. Characteristic green-emitting, luminescent quenching mechanism, and thermometric properties were systematically investigated. Moreover, according to distinct temperature dependence of the characteristic emissions and excitations of Tb^{3+}, both FIR and EIR models were proposed to measure temperature signals.

2 Experimental

In the solid-state preparation route of a Tb^{3+}-incorporated NYTB phosphor, the employed reagents were Na_2CO_3 (analytical reagent (A.R.)), H_3BO_3 (A.R.), Y_2O_3 (99.99%), TeO_2 (99.99%), and Tb_2O_3 (99.99%). Based on the formula of $Na_2Y_{2-x}Tb_xTeO_4(BO_3)_2$ (x = 0–90 mol%), they were weighed, mixed, and ground for 30 min. Subsequently, the obtained mixture was placed in an open muffle furnace (M1210, Henan Chengyi Laboratory Eouipment Co., Ltd.) and preheated at 450 ℃ for 10 h. After preheating, the reactant was ground and sintered at 780 ℃ for 84 h with the grinding at 10 h intervals. The heating rate was 2.5 ℃·min^{-1}. Finally, a white powder sample was prepared after cooling down.

X-ray diffraction (XRD) patterns were characterized by an X-ray diffractometer (DX-2700BH, Bruker; Cu Kα X-ray source with λ = 1.54056 Å). Fourier transform infrared spectroscopy (FTIR) data were collected by an infrared spectrometer (Nicolet iS10, Thermo Scientific). A transmission electron microscope (TEM; JEM 2100, JEOL) was employed to observe morphological features. An elemental investigation was carried out via an energy-dispersive X-ray spectrometer (EscaLab Xi+, FEI) in a scanning electron microscope (SEM; Nova NanoSEM 450, FEI). X-ray photoelectron spectroscopy (XPS) data were recorded by an X-ray photoelectron spectrometer (K-Alpha$^+$, Thermo Fisher Scientific). Diffuse reflectance data were recorded by an ultroviolet/visible (UV/Vis) spectrophotometer (UV2600, SHIMADZU). Luminescent properties were measured by a fluorescence spectrophotometer (F-7100, HITACHI). Electroluminescence (EL) behaviors of a fabricated white light emitting diode (w-LED) device was characterized by an LED optoelectronic analyzer (HP 9000, Hongpu Photoelectric Technology Co., Ltd.).

3 Results and discussion

3. 1 Phase identification

Figure 1(a) displays that the detected XRD profiles of

NYTB:xTb^{3+} (x = 0–90 mol%) coincide well with the standard result of the NYTB (JCPDS No. 66-799). It is suggested that the monoclinic $P2_1/c$ structure of the NYTB is unchanged with the incorporation of the Tb^{3+} ions. Additionally, the ◆ symbol denotes a weak impurity peak coming from $Na_2B_8O_{13}$ (JCPDS No. 71-2163) owing to the secondary reaction. In an NYTB lattice, a coordination number (CN) of the Y^{3+} ion is seven (Fig. 1(b)). The activator Tb^{3+} (CN = 7, radius (r) = 0.98 Å) keeps a similar size as Y^{3+} (CN = 7, r = 0.96 Å) [29], because they belong to a lanthanide group. Thus, the activator Tb^{3+} is inclined to substitute Y^{3+}. Moreover, the magnified XRD peak shifts to a smaller diffraction angle with a Tb^{3+} concentration rising (Fig. 1(a)), which is also the proof that Y^{3+} is substituted by Tb^{3+}. In view of this fact, the following luminescence investigation is uninfluenced by a small amount of $Na_2B_8O_{13}$. Figure 1(c) depicts a Rietveld refinement pattern for a representative sample of the NYTB:70%Tb^{3+}. Residual factors of R_{wp}, R_p, and χ^2 (R_{wp}, R_p, and χ^2 are the refinement results of the weighted profile R-factor, profile residual factor, and goodness-of-fit, respectively) are converged to be 5.02%, 3.58%, and 2.29, respectively, indicating reliability of a monoclinic structure for the prepared sample. Other refined structural data are summarized in Table S1 in the Electronic Supplementary Material (ESM). To explore the impact of incorporating Tb^{3+} on the NYTB lattice, Table 1 summarizes the comparison of the lattice constants for the NYTB and NYTB:70%Tb^{3+}. Clearly, owing to a slightly larger size of Tb^{3+} than that of Y^{3+}, the lattice constants for the NYTB:0.7Tb^{3+} are a little greater than those for the NYTB [28]. On the other hand, FTIR measurements further verify the monoclinic structure of Tb^{3+}-doped samples (Fig. S1 in the ESM). Positions and shapes of the observed vibrations coincide well with those of the NYTB, deriving from ν_{as}(B–O), ν_s(B–O), ν_s(Te–O), ν_b(B–O), and ν(Te–O) in a host lattice [30,31] wherein ν_{as}(B–O) is defined as the asymmetric stretch of the BO_3 groups, ν_s(B–O) is defined as the symmetric stretching vibration of the BO_3 groups, ν_s(Te–O) is defined as the symmetric stretching vibration of the TeO_6 groups, ν_b(B–O) is defined as the bending vibration of the BO_3 groups, and ν(Te–O) is defined as the Te–O antistretching and Te–O–Te vibration. The results mean that structural groups of the NYTB are unbroken even by doping the Tb^{3+} ions.

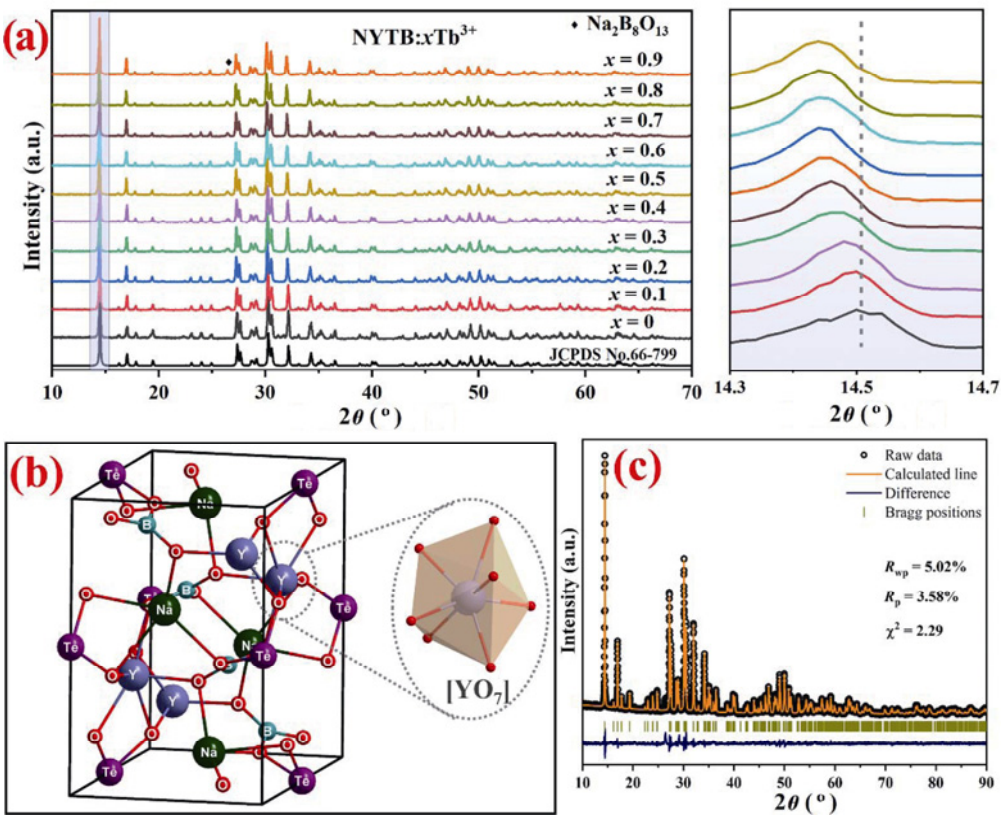

Fig. 1 (a) XRD patterns of NYTB:xTb^{3+} (x = 0–90 mol%) and magnified view of dominant diffraction peak. (b) Crystal structure of NYTB and coordination of Y^{3+}. (c) Rietveld refinement pattern for NYTB:70%Tb^{3+}.

Table 1 Rietveld refinement data for NYTB:70%Tb^{3+}

Sample	NYTB [28]	NYTB:70%Tb^{3+} (this work)
System	Monoclinic	Monoclinic
Space group	$P2_1/c$ (14)	$P2_1/c$ (14)
a (Å)	6.3101	6.3227
b (Å)	9.9363	9.9750
c (Å)	6.7343	6.7547
V (Å^3)	409.286	412.66
Z	2	2
2θ (°)	10–90	10–90
R_{wp} (%)	6.52	5.02
R_p (%)	4.31	3.58
χ^2	3.852	2.29

Note: Z is the number of molecules in a unit cell.

3. 2 Morphological and elemental analysis

The morphology, particle size, and crystallinity of phosphor particles have a significant impact on photoluminescent behaviors. Hereby, the morphological discussion for the studied phosphor is indispensable. According to Fig. 2(a) (scale bar = 30 μm), particle morphology for NYTB:70%Tb^{3+} powder is unevenly shaped. Combined with Fig. 2(b) (scale bar = 3 μm), most of the particles are micron-sized within the range of 3–15 μm, which coincides well with the size requirements of commercial w-LED phosphor particles [32]. Meanwhile, the TEM image discloses a smooth surface of the measured particle (Fig. 2(c)). Figure 2(d) presents the corresponding high-resolution TEM (HRTEM) image with clearly visible lattice fringes. The d-spacing of 3.02 Å corresponds to the $(0\bar{3}1)$ crystal plane of the diffraction peak (2θ = 30.12°), revealing that the studied phosphor maintains good crystallization. According to the elemental investigation (Fig. 2(e)), the NYTB:70%Tb^{3+} powder indeed consists of the

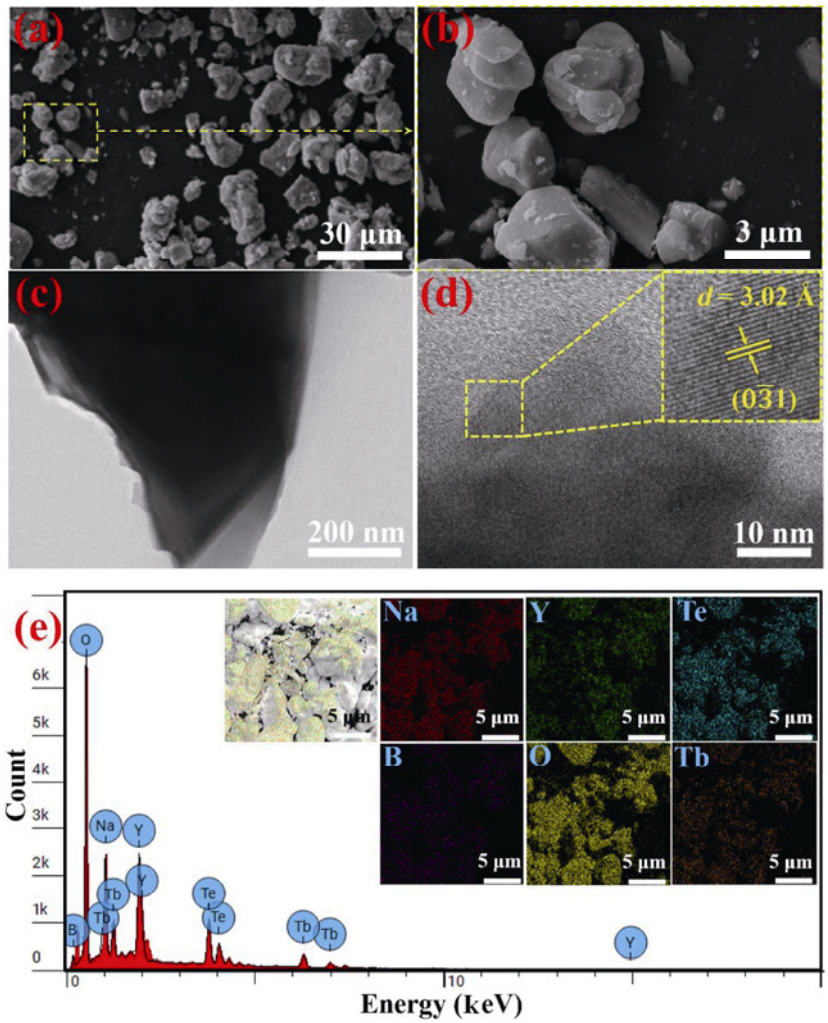

Fig. 2 (a, b) SEM images. (c) TEM image. (d) HRTEM image. (e) Energy-dispersive X-ray spectroscopy (EDS) data for NYTB:70%Tb^{3+} (the inset shows elemental mappings).

elements of Na, Y, Te, B, O, and Tb, which present an even distribution without any additional element.

To accurately determine elemental oxidation states of the representative NYTB:70%Tb^{3+} powder, the corresponding XPS results are illustrated in Fig. 3. A survey scan spectrum shows typical signals of Tb 3d, O 1s, B 1s, Te 3d, Y 3d, and Na 1s (Fig. 3(a)), supporting the obtained EDS data (Fig. 2(e)). For Tb 3d (Fig. 3(b)), the XPS spectrum clearly presents Tb $3d_{5/2}$ (1241.24 eV) and Tb $3d_{3/2}$ (1275.91 eV) peaks with a reasonable binding energy difference (Δ) of 34.67 eV, revealing a +3 oxidation state of terbium [33]. The XPS spectra for Na 1s, B 1s, O 1s, Te 3d, and Y 3d are presented in Fig. S2 in the ESM. The Na 1s peak at 1070.64 eV confirms a +1 valence of sodium [32]. The B 1s peak at 191.47 eV supports a +3 valence of boron [28]. An O 1s spectrum is well-fitted into the three peaks at 530.01, 531.27, and 535.13 eV. The peak with higher binding energy comes from the adsorbed oxygen [32], and the other peaks result from the lattice oxygen bonding with sodium, yttrium, tellurium, boron, and terbium [34]. For Te 3d, the Te $3d_{5/2}$ (576.08 eV) and Te $3d_{3/2}$ (586.46 eV) peaks with Δ = 10.38 eV demonstrate a +6 valence of tellurium [31]. For Y 3d, the Y $3d_{5/2}$ (157.29 eV) and Y $3d_{3/2}$ (159.35 eV) peaks have the Δ value of 2.06 eV, manifesting a +3 valence of yttrium [28].

3. 3 Photoluminescence (PL) properties

Figure 4(a) exhibits diffuse reflectance curves of the NYTB:$x$$Tb^{3+}$ (x = 0–90 mol%). Charge transitions of a NYTB host cause the strong absorption below 300 nm,

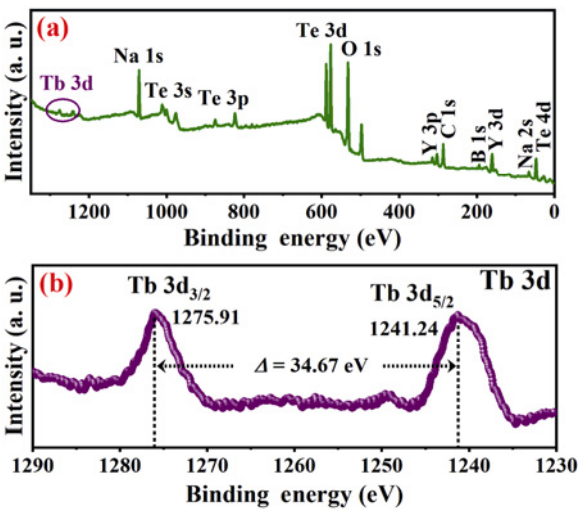

Fig. 3 (a) XPS survey scan spectrum. (b) Core-level spectrum of Tb 3d for NYTB:70%Tb^{3+}.

including the two absorption band peaks at 217 and 284 nm. For the pure NYTB host, apart from a deep ultraviolet absorption band, there is no other absorption. For the Tb^{3+}-doped samples, the obtained absorption peaks at 378 and 487 nm are due to the $^7F_6 \rightarrow {}^5D_3$ and $^7F_6 \rightarrow {}^5D_4$ transitions of Tb^{3+}, respectively (the inset of Fig. 4(a)) [35]. Moreover, their intensity is gradually enhanced with the doping Tb^{3+} ions, which would further support the truth that the Tb^{3+} ions are successfully introduced into the NYTB lattice. According to the diffuse reflectance data, the Tb^{3+} content-dependent band gap (E_g) was determined. The E_g values are 3.54, 3.71, 3.67, 3.65, 3.67, 3.66, 3.67, 3.66, 3.66, and 3.70 eV, corresponding to x = 0, 10, 20, 30, 40, 50, 60, 70, 80, and 90 mol%, respectively (Fig. 4(b)), which are similar to those reported by Feng *et al*. [30]. Varying the Tb^{3+} contents have almost no impact on E_g of the Tb^{3+}-activated NYTB phase, indicating that the prepared samples have good crystallization and few defects.

We used λ = 378 nm ($^7F_6 \rightarrow {}^5D_3$ of Tb^{3+}) to irradiate the NYTB:$x$$Tb^{3+}$ (x = 10–90 mol%) powder samples, according to PL excitation (PLE) curves (Fig. S3 in the ESM). The obtained PL spectra are illustrated in Fig. 5(a). Five PL components (497, 547, 585, 624, and 648 nm) come from the electronic transitions of Tb^{3+} between a excited state ($^5D_4$) and ground states ($^7F_6$, $^7F_5$, $^7F_4$, $^7F_3$, and $^7F_2$, respectively) [36]. Even though the Tb^{3+} contents vaired, the shapes and positions of the emissions are unchanged besides the intensity. Integral PL intensity is dependent on the Tb^{3+} content, as given in Fig. 5(b). The intensity presents an optimum value, corresponding to x = 70 mol%. Subsequently, when the Tb^{3+} content exceeds 70 mol%, the intensity drops due to content-dependent luminescence quenching [37]. Moreover, a variation trend for the integral PL intensity excited at 487 nm (Fig. S4 in the ESM) is consistent with the results in Fig. 5(b). On the other hand, the PLE measurement also shows that the 70 mol% Tb^{3+} content is the optimal (Fig. S3 in the ESM). The results support reliability of luminescent data. Such high Tb^{3+} content added into host materials has been also reported, such as $Ca_9Y(PO_4)_7$:Tb^{3+} [38] and $Sr_3Gd(PO_4)_3$:Tb^{3+} [39].

Considering that there are generally re-absorption, exchange interaction, and multipolar interaction-induced concentration quenching [40], first of all, we compared the PL with the PLE of the representative NYTB:70% Tb^{3+} sample. The overlap with the range of 475–500 nm is observed (Fig. S5 in the ESM), revealing the probability of re-absorption. Subsequently, Blasse theory [41] was

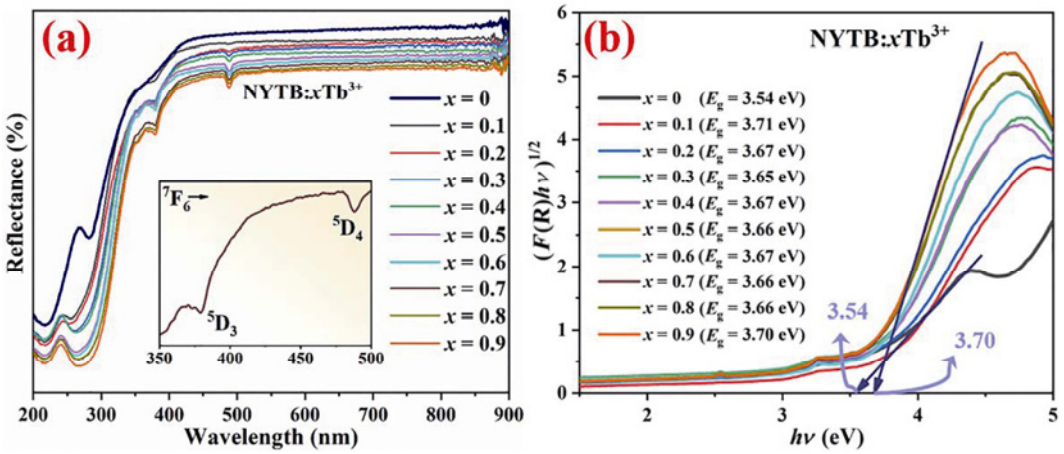

Fig. 4 (a) Diffuse reflectance spectra (the inset shows a magnified part in 350–500 nm for representative NYTB:70%Tb^{3+} sample). (b) E_g for NYTB:$x$$Tb^{3+}$ (x = 0–90 mol%).

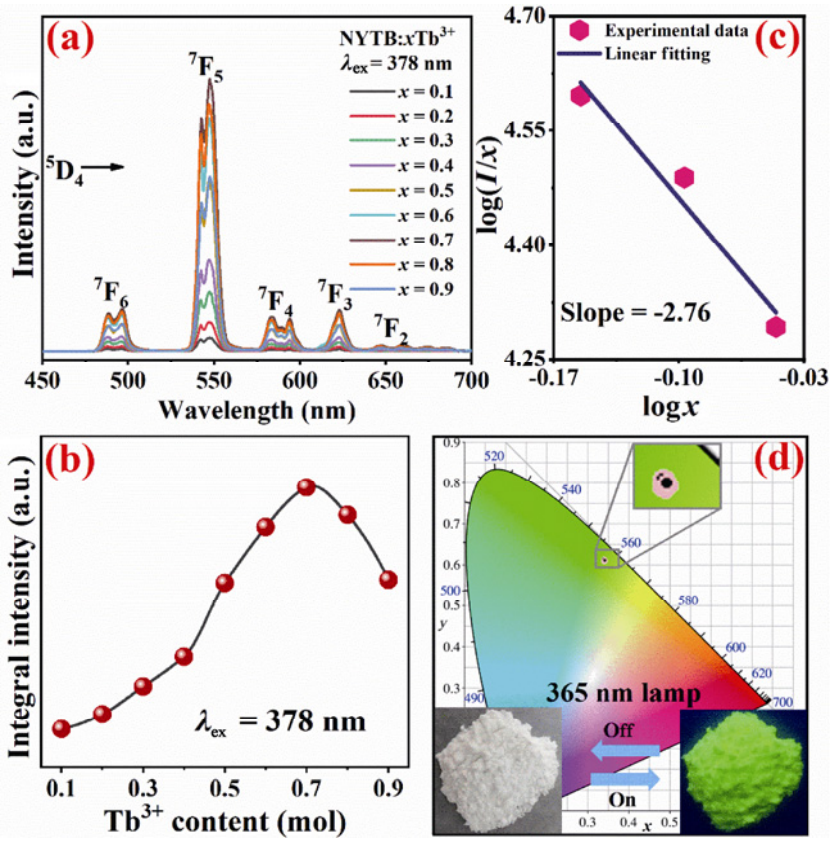

Fig. 5 (a) PL spectra of NYTB:$x$$Tb^{3+}$ (x = 10–90 mol%) excited at 378 nm. (b) Tb^{3+} content-dependent PL intensity. (c) Plot of log(I/x) vs. log$x$. (d) CIE chromaticity diagram (the insets illustrate digital photos of respective NYTB:70%Tb^{3+} sample excited by 365 nm lamp). Note: λ_{ex} represents the excitation wavelength.

employed to discuss the critical distance (R_c) among the Tb^{3+} ions. In this system, the R_c value (6.55 Å) is larger than 5 Å, indicating that the non-radiative energy transfer is ascribed to the multipolar interaction rather than the exchange interaction. Finally, the log$x$ dependence of log(I/x) was explored by a Dexter model (Eq. (S1) in the ESM) [42], as depicted in Fig. 5(c). The slope (−2.76) of the fitting line means that θ = 8.28, demonstrating that the concentration quenching is caused by the dipole–quadrupole interaction. As analyzed above, both re-absorption and dipole–quadrupole interaction contribute to the luminescent concentration quenching.

Based on the PL data excited at 378 nm, chromatic coordinates of the representative NYTB:70%Tb^{3+}

phosphor were obtained, which are located in the green region (Fig. 5(d)). The inset of Fig. 5(d) shows an image of a green-emitting sample excited by a portable 365 nm lamp. The Tb^{3+} concentration-dependent chromatic coordinates are summarized in Table 2. The coordinates are slightly changed with the increasing Tb^{3+} ions, falling into the green region. Moreover, color purity (CP) is calculated by Eq. (S2) in the ESM. The CP values are above 73% (Table 2), which is well comparable to the data of the Tb^{3+}-activated phosphors reported such as 73% for Bi_3TeBO_9:0.11Tb^{3+} [31], 19.8% for $Sr_3Gd(PO_4)_3$:0.01Tb^{3+} [39], 68% for $Ba_3(ZnB_5O_{10})PO_4$:0.07Tb^{3+} [43], 64.13% for $CaLa_4Si_3O_{13}$:0.07Tb^{3+} [44], and 86% for $Na_3La_{0.92}(VO_4)_2$:0.08Tb^{3+} [45].

Figure 6(a) shows decay curves (λ_{ex} = 378 nm and the emission wavelength (λ_{em}) = 547 nm) of the NYTB:$x$$Tb^{3+}$ (x = 10–90 mol%) phosphors, which could be fitted by a two-exponential model by Eq. (S3) in the ESM. The results indicate the presence of two Tb^{3+} emitting centers. Tb^{3+} activators have a seven-fold coordination by replacing Y^{3+} ions. Besides, a part of Tb^{3+} activators probably substitute Na^{+} ions or appear at a surface of the powder particles due to the high Tb^{3+} concentration [46,47]. Rapid, slow, and average decay time (marked as τ_1, τ_2, and τ_{ave}, respectively) are listed in Table S2 in the ESM. The τ_{ave} value gradually decreases with the increasing Tb^{3+} concentration (Fig. 6(b)), originating from the increased non-radiative transition among Tb^{3+} ions. Besides, quantum efficiency is a significant parameter for the phosphor materials. Hereby, internal quantum efficiency (IQE) and external quantum efficiency (EQE) of the NYTB:70%Tb^{3+} are measured and estimated by Eq. (S4) in the ESM. The IQE and EQE values are determined to be 46.4%, and 6.7%, respectively (Fig. 6(c)). Finally, we constructed

Table 2 Chromaticity coordinates and CP of NYTB:$x$$Tb^{3+}$ (x = 10–90 mol%)

x (mol%)	Coordinate (x, y)	CP (%)
10	(0.3396, 0.6079)	73.5
20	(0.3386, 0.6095)	74.0
30	(0.3390, 0.6108)	74.5
40	(0.3391, 0.6116)	74.8
50	(0.3405, 0.6117)	74.8
60	(0.3422, 0.6110)	74.7
70	(0.3419, 0.6131)	75.7
80	(0.3392, 0.6146)	75.6
90	(0.3419, 0.6120)	75.5

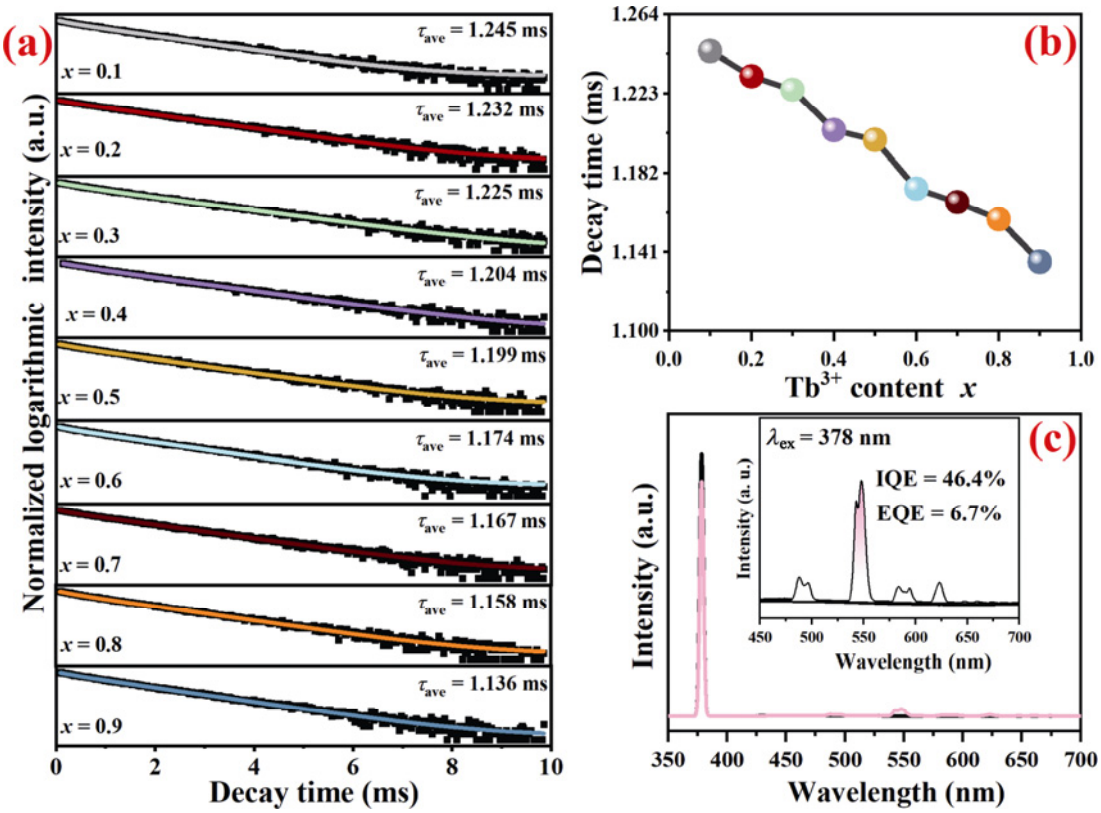

Fig. 6 (a) Decay curves of NYTB:$x$$Tb^{3+}$ (x = 10–90 mol%). (b) Decay time in response to Tb^{3+} content. (c) IQE and EQE of NYTB:70%Tb^{3+}.

a w-LED device (Fig. S6 in the ESM), in which the studied NYTB:70%Tb^{3+} phosphor is combined with a near-UV (NUV) chip (380 nm) and commercial phosphors ($BaMgAl_{10}O_{17}$ (BAM):Eu^{2+} (blue) and (Ca,Sr)$AlSiN_3$:Eu^{2+} (red)). Driven by a current of 100 mA, the w-LED device emits bright white light with R_a = 85, CCT = 5125 K, and the CIE = (0.3413, 0.3427) where R_a is the color render index, and CCT is the correlated color temperature. However, the temperature dependence of the PL spectra for the NYTB:70%Tb^{3+} reveals weak luminescent thermostability (Fig. S7 in the ESM). The results also indicate a potential optical temperature sensing behavior for the studied phosphor.

3. 4 Temperature sensing properties

The temperature dependence of the PL spectra for the NYTB:70%Tb^{3+} shows that the integral intensity descends dramatically with the rising temperature (Fig. S7 in the ESM). Notably, in the range of 300–475 K, the decreasing trends of 497 nm ($^5D_4 \rightarrow {}^7F_6$), 547 nm ($^5D_4 \rightarrow {}^7F_5$), and 585 nm ($^5D_4 \rightarrow {}^7F_4$) peaks are various, as given in Fig. S10 in the ESM. The PL intensity at 547 nm decreases markedly, whereas those at 497 and 585 nm descend slowly. The results reveal the feasibility of detecting the temperature signals based on the FIR among these peaks. Figures 7(a) and 7(c) illustrate the FIR(I_{497}/I_{547}) and FIR(I_{585}/I_{547}) as a function of the temperature, respectively, which are fitted via a semi-exponential model (Eq. (S5) in the ESM). The high R^2 values (R^2 = 0.997 for the FIR(I_{497}/I_{547}) and 0.999 for the FIR(I_{585}/I_{547})) mean the reliability of the fitting results. Subsequently, to further evaluate the temperature sensing properties, S_A and S_R are obtained by Eqs. (S6) and (S7) in the ESM, respectively. The S_R and S_A data for the FIR(I_{497}/I_{547}) and FIR(I_{585}/I_{547}) in response to the temperature are given in Figs. 7(b) and 7(d), respectively. Both S_R and S_A values at 300 K reach the maximum ($S_{R\text{-max}}$ = 5.23 %·K^{-1} and $S_{A\text{-max}}$ = 1.01×10^{-2} K^{-1} for the FIR(I_{497}/I_{547}); $S_{R\text{-max}}$ = 5.74 %·K^{-1} and $S_{A\text{-max}}$ = 1.02×10^{-2} K^{-1} for the FIR(I_{585}/I_{547})).

The temperature resolution (δT) is a key parameter for the luminescent thermometry, which is determined by Eq. (S8) in the ESM. To obtain an accurate δFIR/FIR, the FIR(I_{497}/I_{547}) value was measured about thirty times, as shown in Fig. 8(a). Based on the standard deviation, the δFIR/FIR for the FIR(I_{497}/I_{547}) is defined as 0.1%. The δT values are 0.019 and

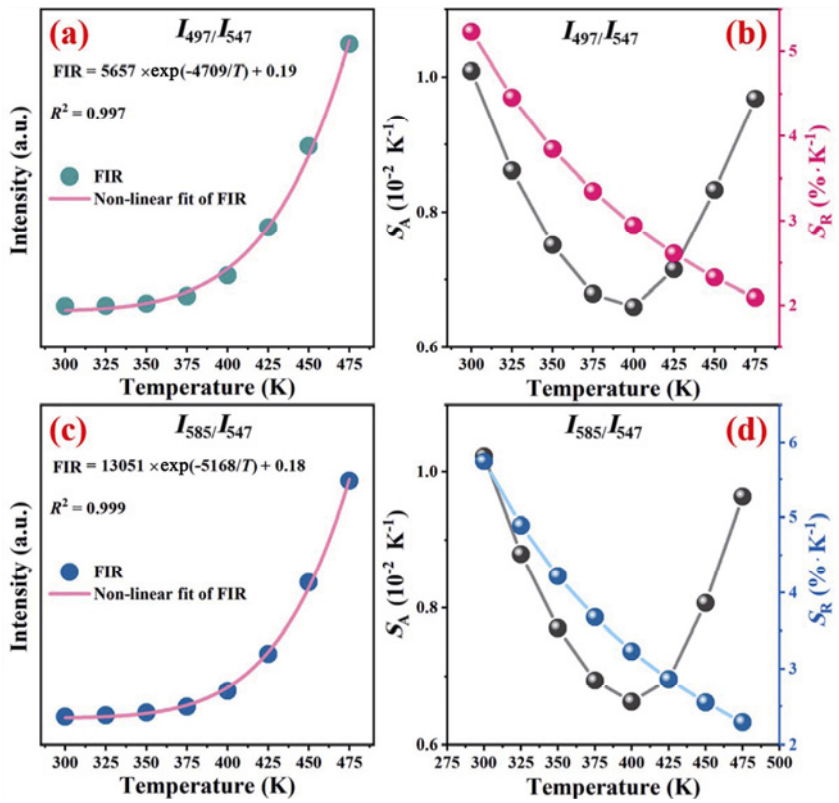

Fig. 7 (a) Variation of FIR(I_{497}/I_{547}). (b) Changes of S_A and S_R for FIR(I_{497}/I_{547}). (c) Variation of FIR(I_{585}/I_{547}). (d) Changes of S_A and S_R for FIR(I_{585}/I_{547}) in response to temperature.

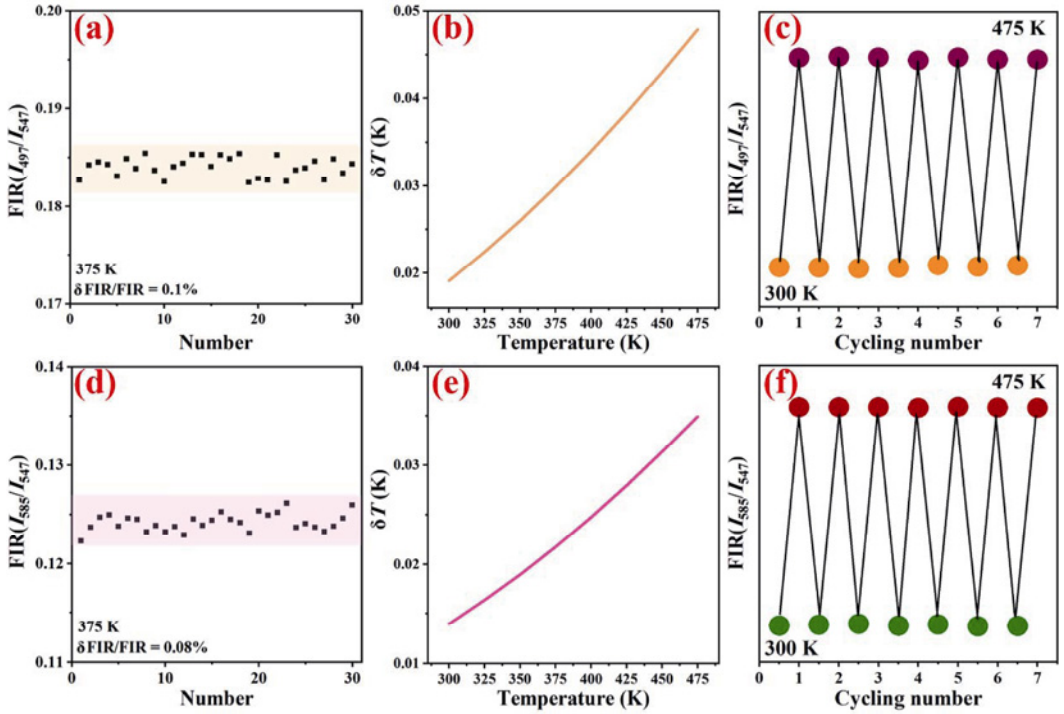

Fig. 8 (a) Thirty measurements of FIR(I_{497}/I_{547}). (b) δT of FIR(I_{497}/I_{547}). (c) Thermal repeatability of FIR(I_{497}/I_{547}) between 300 and 475 K. (d) Thirty measurements of FIR(I_{585}/I_{547}). (e) δT of FIR(I_{585}/I_{547}). (f) Thermal repeatability of FIR(I_{585}/I_{547}) between 300 and 475 K.

0.048 K at 300 and 475 K, respectively (Fig. 8(b)). Meanwhile, the thermal repeatability (R) is performed by temperature cycle measurements under the same conditions, which show excellent repeatability and reversibility after seven cycling experiments, as displayed in Fig. 8(c). Figure S9(a) in the ESM shows the one temperature cycle measurement PL spectra. The PL spectra of heating match well with the PL spectra of cooling. In the thermal cycle, the FIR(I_{497}/I_{547}) values return to the original strength (Fig. S9(b) in the ESM). Additionally, the δFIR/FIR for the FIR(I_{585}/I_{547}) is defined as 0.08% (Fig. 8(d)). The δT value is changed from 0.014 to 0.035 K at the rising temperatures from 300 to 475 K (Fig. 8(e)). Figure 8(f) shows a temperature cycle process, which exhibits good repeatability for a FIR(I_{585}/I_{547}) model. Meanwhile, the one cycle of the FIR(I_{585}/I_{547}) model is presented in Fig. S9(c) in the ESM, indicating excellent repeatability for luminescent thermometric applications.

In addition, based on the PLE data of the NYTB: 70%Tb^{3+} phosphor in response to the temperature (Fig. S10 in the ESM), the thermometric properties were also discussed. The EIR between the peaks at 378 nm ($^7F_6 \rightarrow {}^5D_3$) and 487 nm ($^7F_6 \rightarrow {}^5D_4$) is applied to the excited state thermometry. Figure 9(a) shows a variation of the EIR in response to the temperature, which was fitted by Eq. (S5) in the ESM. The fitting results are reasonable due to $R^2 = 0.999$. Equations (S6) and (S7) in the ESM are employed to evaluate S_A and S_R for the EIR(I_{378}/I_{487}), respectively. According to Fig. 9(b), the largest S_R and S_A values are 2.49 %·K^{-1} and 2.16×10^{-2} K^{-1}, respectively.

Similarly, the δEIR/EIR and δT values for the EIR model are evaluated, as shown in Figs. 10(a) and 10(b), respectively. The δEIR/EIR is determined as 0.38%. The δT value is changed from 0.15 to 0.38 K upon the rising temperatures from 300 to 475 K. The temperature cycle process is carried out to assess the repeatability and reversibility. Figure 10(c) displays excellent repeatability of the EIR model. The PLE spectra in the one temperature cycle measurement show a similar trend, revealing good repeatability and reversibility for the EIR model (Fig. S11 in the ESM).

Based on the FIR/EIR model, in contrast to some reported thermometric materials, the NYTB:70%Tb^{3+} phosphor demonstrates satisfactory S_R and S_A parameters, as listed in Table 3. Compared with the FIR model, the EIR-based temperature sensing technology for rare-earth-ion-activated phosphors is insufficiently investigated. Moreover, there are few thermometric materials reported, which can present the thermometric properties based on both FIR and EIR technologies.

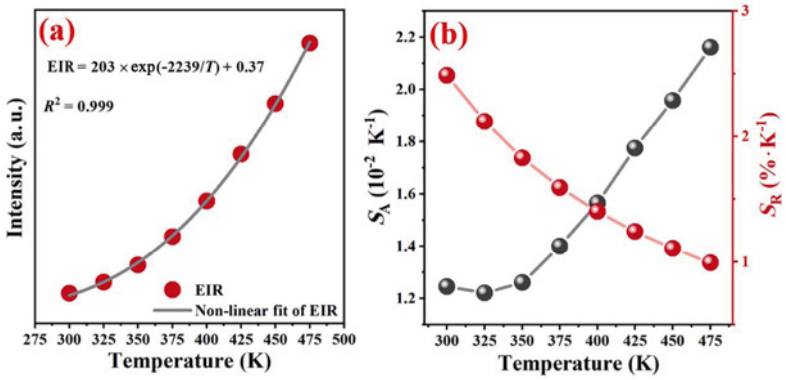

Fig. 9 (a) Variation of EIR. (b) Changes of S_A and S_R in response to temperature.

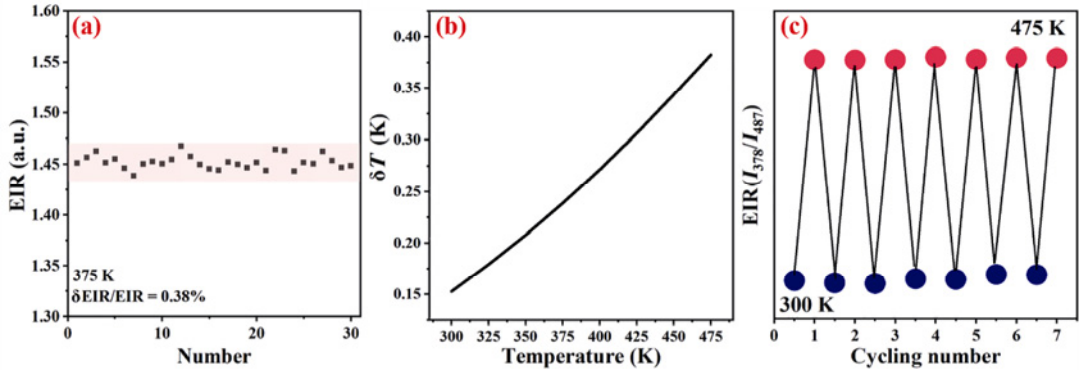

Fig. 10 (a) Thirty measurements of EIR. (b) δT of EIR(I_{378}/I_{487}). (c) Thermal repeatability between 300 and 475 K.

Table 3 $S_{R\text{-max}}$ **and** $S_{A\text{-max}}$ **parameters of reported thermometric materials**

Material	Model	$S_{R\text{-max}}$ (%·K^{-1})	$S_{A\text{-max}}$ (10^{-2} K^{-1})	T (K)	Ref.
$YVO_4:Eu^{3+}$	EIR	1.19	0.038	298–473	[10]
$KLaP_4O_{12}:Tb^{3+}$	EIR	5.5	—	273–473	[23]
$La_2ZnTiO_6:Tb^{3+}$	EIR	0.734	4.46	293–573	[27]
$Ca_2LaNbO_6:Sm^{3+}$	EIR	0.28	—	313–573	[48]
$CaWO_4:Nd^{3+}$	EIR	0.96	0.939	298–573	[49]
$K_3LuSi_2O_7:Eu^{3+}$	EIR	0.539	2.03	313–573	[50]
NYTB:Tb^{3+}	EIR	2.49	2.16	300–475	This work
$YVO_4:Eu^{3+}$	FIR	1.28	0.581	298–466	[10]
$Ca_2LaNbO_6:Sm^{3+}$	FIR	0.23	—	313–573	[48]
$LaMg_{0.402}Nb_{0.598}O_3:Pr^{3+}$	FIR	0.83	6	298–523	[51]
$NaLuF_4:Eu^{3+}$@g-C_3N_4	FIR	0.455	5.7	303–503	[52]
$CaWO_4:Tb^{3+}$	FIR	1.21	—	343–783	[53]
$LuNbO_4:Pr^{3+}/Tb^{3+}$	FIR	1.26	2.4	283–493	[54]
$Ba_{1.5}Sr_{0.5}Ga_4O_8:Bi^{3+}$	FIR	1.295	0.5	7–400	[55]
$CaBaZn_2Ga_2O_7:Bi^{3+}$	FIR	1.453	15.4	298–473	[56]
$Sr_2LaF_7:Er^{3+}$	FIR	0.639	40.9	303–433	[57]
$LaTiSbO_6:Mn^{4+}$/YAG:Ce^{3+}–PiG	FIR	1.61	3.58	273–418	[58]
$Y_2MgTiO_6:Mn^{4+}$	FIR	0.142	—	10–513	[59]
$MgTiO_3:Mn^{4+}$	FIR	1.2	—	133–363	[60]
$SrAl_{12}O_{19}:Mn^{4+}$	FIR	0.27	0.4	273–393	[61]
$CaNb_2O_6:Bi^{3+}/Eu^{3+}$	FIR	3.793	12.2	298–523	[62]
$Gd_2ZnTiO_6:Bi^{3+},Mn^{4+}$	FIR	2.4	16.8	313–473	[63]
NYTB:Tb^{3+}	FIR	5.74	1.02	300–475	This work

Note: YAG and PiG represent $Y_3Al_5O_{12}$ and phosphor-in-glass, respectively.

4 Conclusions

In summary, NYTB:xTb^{3+} (x = 10–90 mol%) phosphors were developed by a solid-state reaction. The luminescent content quenching mechanism is determined. Under the excitation at 378 nm, the representative NYTB: 70%Tb^{3+} phosphor shows green light with the coordinates of (0.3419, 0.6131) and an IQE of 46.4%. Importantly, the excellent thermometric properties for the NYTB:70%Tb^{3+} are illustrated based on the proposed FIR/EIR model. The obtained $S_{R\text{-}max}/S_{A\text{-}max}$ for the FIR(I_{497}/I_{547}), FIR(I_{585}/I_{547}), and EIR(I_{487}/I_{378}) signals are (5.23 %·K^{-1}/1.01×10^{-2} K^{-1}), (5.74 %·K^{-1}/1.02×10^{-2} K^{-1}), and (2.49 %·K^{-1}/2.16×10^{-2} K^{-1}), respectively. The good δT and repeatability are confirmed. The results suggest that the studied phosphor is a well-performing FIR-/EIR-based thermometric material. This work provides a new perspective on the noncontact optical thermometry based on the FIR/EIR technologies.

Acknowledgements

This work was financially supported by the National Natural Science Foundation of China (No. 22165031), National Undergraduate Innovation and Entrepreneurship Foundation (Nos. 202210673034 and 202210673052), and Program for Excellent Young Talents, Yunnan University. We thank Advanced Analysis and Measurement Center of Yunnan University for the sample testing service.

Declaration of competing interest

The authors have no competing interests to declare that are relevant to the content of this article.

Electronic Supplementary Material

Supplementary material is available in the online version of this article at https://doi.org/10.26599/JAC.2023.9220725.

References

[1] Li L, Zhang C, Xu L, *et al*. Luminescence ratiometric nanothermometry regulated by tailoring annihilators of triplet–triplet annihilation upconversion nanomicelles. *Angew Chem Int Ed* 2021, **60**: 26725–26733.

[2] Kourtellaris A, Lafargue-Dit-Hauret W, Massuyeau F, *et al*. Tuning of thermometric performances of mixed Eu–Tb metal–organic frameworks through single-crystal coordinating solvent exchange reactions. *Adv Opt Mater* 2022, **10**: 2200484.

[3] Chen YB, He J, Zhang XG, *et al*. Dual-mode optical thermometry design in $Lu_3Al_5O_{12}$:Ce^{3+}/Mn^{4+} phosphor. *Inorg Chem* 2020, **59**: 1383–1392.

[4] Ye YC, Lu KL, Qi JQ. Developing smart temperature sensing window based on highly transparent rare-earth doped yttrium zirconate ceramics. *ACS Appl Mater Interfaces* 2022, **14**: 39072–39080.

[5] Stefańska J, Bednarkiewicz A, Marciniak L. Advancements in excited state absorption-based luminescence thermometry. *J Mater Chem C* 2022, **10**: 5744–5782.

[6] Kolesnikov IE, Mamonova DV, Kurochkin MA, *et al*. Double-doped YVO_4 nanoparticles as optical dual-center ratiometric thermometers. *Phys Chem Chem Phys* 2022, **24**: 15349–15356.

[7] Ghahrizjani RT, Ghafarkani M, Janghorban S, *et al*. ZnO–$SrAl_2O_4$:Eu nanocomposite-based optical sensors for luminescence thermometry. *ACS Appl Nano Mater* 2021, **4**: 9190–9199.

[8] Cheng Y, Gao Y, Lin H, *et al*. Strategy design for ratiometric luminescence thermometry: Circumventing the limitation of thermally coupled levels. *J Mater Chem C* 2018, **6**: 7462–7478.

[9] Cui JR, Li YY, Li HY, *et al*. Synthesis of Tb^{3+} doped $SrMoO_4/SiO_2$ nanophosphor and its sensing properties for inorganic ions and tyrosine. *Microchem J* 2022, **181**: 107736.

[10] Kolesnikov IE, Kalinichev AA, Kurochkin MA, *et al*. Ratiometric optical thermometry based on emission and excitation spectra of YVO_4:Eu^{3+} nanophosphors. *J Phys Chem C* 2019, **123**: 5136–5143.

[11] Fang ZY, Yang D, Zheng YK, *et al*. NUV-pumped luminescence of thermally stable samarium-activated alkali metal borophosphate phosphor. *J Adv Ceram* 2021, **10**: 1072–1081.

[12] Wang Q, Liao M, Lin QM, *et al*. A review on fluorescence intensity ratio thermometer based on rare-earth and transition metal ions doped inorganic luminescent materials. *J Alloys Compd* 2021, **850**: 156744.

[13] Hua YB, Yu JS. Strong green emission of erbium(III)-activated La_2MgTiO_6 phosphors for solid-state lighting and optical temperature sensors. *ACS Sustainable Chem Eng* 2021, **9**: 5105–5115.

[14] Jahanbazi F, Mao YB. Recent advances on metal oxide-based luminescence thermometry. *J Mater Chem C* 2021, **9**: 16410–16439.

[15] Zhao Y, Wang XS, Zhang Y, *et al*. Optical temperature sensing of up-conversion luminescent materials: Fundamentals and progress. *J Alloys Compd* 2020, **817**: 152691.

[16] Jin H, Jiang XW, Sun ZJ, *et al*. Phosphorescence-based ratiometric probes: Design, preparation and applications in sensing, imaging and biomedicine therapy. *Coordin Chem Rev* 2021, **431**: 213694.

[17] Katumo N, Gao GJ, Laufer F, *et al*. Smartphone-based luminescent thermometry via temperature-sensitive delayed

fluorescence from $Gd_2O_2S:Eu^{3+}$. *Adv Opt Mater* 2020, **8**: 2000507.

[18] Diaz-Rodriguez RM, Gálico DA, Chartrand D, *et al*. Toward opto-structural correlation to investigate luminescence thermometry in an organometallic Eu(II) complex. *J Am Chem Soc* 2022, **144**: 912–921.

[19] Lal SC, Naseemabeevi JI, Ganesanpotti S. Distortion induced structural characteristics of $Ba_2R_{2/3}TeO_6$ (R = Y, Gd, Tb, Dy, Ho, Er, Tm, Yb and Lu) double perovskites and their multifunctional optical properties for lighting and ratiometric temperature sensing. *Mater Adv* 2021, **2**: 1328–1342.

[20] Qiu LT, Mao JS, Zhao ZM, *et al*. Temperature sensing properties of self-crystalized $Ba_2LaF_7:Tb^{3+}$ glass ceramics. *Ceram Int* 2021, **47**: 6244–6250.

[21] Hu FF, Gong HL, Ashraf GA, *et al*. Novel transparent Tb^{3+}-activated Na_2GdF_7 glass ceramics for low-lying state thermal coupling principle. *J Alloys Compd* 2022, **909**: 164776.

[22] Drabik J, Lisiecki R, Marciniak L. Optimization of the thermometric performance of single band ratiometric luminescent thermometer based on Tb^{3+} luminescence by the enhancement of thermal quenching of GSA-excited luminescence in TZPN glass. *J Alloys Compd* 2021, **858**: 157690.

[23] Drabik J, Marciniak L. $KLaP_4O_{12}:Tb^{3+}$ nanocrystals for luminescent thermometry in a single-band-ratiometric approach. *ACS Appl Nano Mater* 2020, **3**: 3798–3806.

[24] Wei ZT, Chen WB, Wang ZQ, *et al*. High-temperature persistent luminescence and visual dual-emitting optical temperature sensing in self-activated $CaNb_2O_6:Tb^{3+}$ phosphor. *J Am Ceram Soc* 2021, **104**: 1750–1759.

[25] Li YY, Zhou YY, Li X, *et al*. Energy transfer and the anti-thermal quenching behavior of $Sr_8MgCe(PO_4)_7:Tb^{3+}$ for temperature sensing. *Spectrochim Acta A* 2021, **252**: 119548.

[26] Drabik J, Ledwa K, Marciniak Ł. Implementing defects for ratiometric luminescence thermometry. *Nanomaterials* 2020, **10**: 1333.

[27] Li JW, Wang JW, Lei RS, *et al*. Ratiometric luminescence thermometry based on diverse thermal response from excited states in $La_2ZnTiO_6:Tb^{3+}$. *J Lumin* 2022, **249**: 119047.

[28] Xiang YF, Zheng YK, Yang L, *et al*. Exploring a new Dy^{3+}-activated borotellurate phosphor with thermally stable photoluminescence. *J Alloys Compd* 2022, **919**: 165837.

[29] Shannon RD. Revised effective ionic radii and systematic studies of interatomic distances in halides and chalcogenides. *Acta Crystallogr A* 1976, **32**: 751–767.

[30] Feng JH, Hu CL, Xu X, *et al*. $Na_2RE_2TeO_4(BO_3)_2$ (RE = Y, Dy–Lu): Luminescent and structural studies on a series of mixed metal borotellurates. *Inorg Chem* 2015, **54**: 2447–2454.

[31] Song JL, Li H, Xiang YF, *et al*. Content and temperature quenching of Tb^{3+}-activated Bi_3TeBO_9 green phosphor excited by NUV/Vis light. *J Solid State Chem* 2022, **313**: 123317.

[32] Xiang JY, Fang ZY, Yang D, *et al*. Optimizational orange emitting behavior of $Li_2Na_{1-x}BP_2O_8:x$Pr solid solutions under an short-wave ultraviolet irradiation. *Scripta Mater* 2020, **187**: 82–87.

[33] Shimono S, Izaki T, Tanaka N, *et al*. Crystal structure, luminescence, and thermal stability of $CsAlSi_2O_6:Tb^{3+}$ phosphors with highly efficient green emission. *Mater Res Bull* 2021, **143**: 111441.

[34] Li Q, Wang Y, Wang J, *et al*. High transparency $Pr:Y_2O_3$ ceramics: A promising gain medium for red emission solid-state lasers. *J Adv Ceram* 2022, **11**: 874–881.

[35] Zhu J, Xiang JY, Mao Y. Near-UV-excited photoluminescence of terbium (Ⅲ)-activated lithium sodium borophosphate phosphor. *Optik* 2021, **240**: 166920.

[36] Gupta SK, Ghosh PS, Yadav AK, *et al*. Luminescence properties of $SrZrO_3/Tb^{3+}$ perovskite: Host-dopant energy-transfer dynamics and local structure of Tb^{3+}. *Inorg Chem* 2016, **55**: 1728–1740.

[37] Wang SY, Devakumar B, Sun Q, *et al*. Highly efficient near-UV-excitable $Ca_2YHf_2Al_3O_{12}:Ce^{3+},Tb^{3+}$ green-emitting garnet phosphors with potential application in high color rendering warm-white LEDs. *J Mater Chem C* 2020, **8**: 4408–4420.

[38] Siwach A, Kumar D. Structural and optical behavior of nano-scaled luminous green-emitting $Ca_9Y(PO_4)_7:Tb^{3+}$ phosphor for competent lighting devices. *Chem Phys Lett* 2021, **772**: 138547.

[39] Jamalaiah BC, Khan PS, Madhu N, *et al*. Green luminescent $Sr_3Gd(PO_4)_3:Tb^{3+}$ phosphors for lighting applications. *Ceram Int* 2022, **48**: 28927–28934.

[40] Liu YF, Zhang JX, Zhang CH, *et al*. High efficiency green phosphor $Ba_9Lu_2Si_6O_{24}:Tb^{3+}$: Visible quantum cutting via cross-relaxation energy transfers. *J Phys Chem C* 2016, **120**: 2362–2370.

[41] Blasse G. Energy transfer in oxidic phosphors. *Phys Lett A* 1968, **28**: 444–445.

[42] Li JY, Zhou XF, Ding JY, *et al*. Mechanism analysis of a narrow-band ultra-bright green phosphor with its prospect in white light-emitting diodes and field emission displays. *J Mater Chem C* 2019, **7**: 2257–2266.

[43] Zheng YK, Yang TS, Xiang YF, *et al*. $Ba_3(ZnB_5O_{10})PO_4:Tb^{3+}$ green phosphor: Microwave-assisted sintering synthesis and thermally stable photoluminescence. *J Alloys Compd* 2022, **911**: 165087.

[44] Singh V, Kadam AR, Dhoble SJ, *et al*. Luminescence studies of green emitting $CaLa_4Si_3O_{13}:Tb^{3+}$ phosphor for wLED and PDP applications. *Optik* 2021, **243**: 167327.

[45] Zhao D, Liu W, Li YN, *et al*. (3+1)-dimensional modulated structure and Tb^{3+}-doped luminescence for vanadate $Na_3La(VO_4)_2$. *Inorg Chem* 2022, **61**: 6311–6318.

[46] Zhang XM, Seo HJ. Photoluminescence and concentration quenching of $NaCa_4(BO_3)_3:Eu^{3+}$ phosphor. *J Alloys Compd* 2010, **503**: L14–L17.

[47] Zhezhera T, Gluchowski P, Nowicki M, *et al*. Efficient near-infrared quantum cutting by cooperative energy transfer in $Bi_3TeBO_9:Nd^{3+}$ phosphors. *J Mater Sci* 2022, **57**: 185–203.

[48] Zhang AQ, Sun Z, Jia MC, *et al*. Sm^{3+}-doped niobate orange–red phosphors with a double-perovskite structure for plant cultivation and temperature sensing. *J Alloys Compd* 2021, **889**: 161671.

[49] Chang QY, Zhou XJ, Zhou X, *et al*. Strategy for optical thermometry based on temperature-dependent charge transfer to the Eu^{3+} 4f–4f excitation intensity ratio in $Sr_3Lu(VO_4)_3$:Eu^{3+} and $CaWO_4$:Nd^{3+}. *Opt Lett* 2020, **45**: 3637–3640.

[50] Feng JY, Wang ZY, Xu HY, *et al*. The charge transfer band as a key to study the site selection preference of Eu^{3+} in inorganic crystals. *Inorg Chem* 2021, **60**: 19440–19447.

[51] Zhang H, Gao ZY, Li GG, *et al*. A ratiometric optical thermometer with multi-color emission and high sensitivity based on double perovskite $LaMg_{0.402}Nb_{0.598}O_3$:$Pr^{3+}$ thermochromic phosphors. *Chem Eng J* 2020, **380**: 122491.

[52] Du P, Tang J, Li WP, *et al*. Exploiting the diverse photoluminescence behaviors of $NaLuF_4$:xEu^{3+} nanoparticles and g-C_3N_4 to realize versatile applications in white light-emitting diode and optical thermometer. *Chem Eng J* 2021, **406**: 127165.

[53] Li LP, Qin F, Li L, *et al*. Thermal enhancement of the green luminescence of Tb^{3+} ion generated by ground state thermal population. *J Lumin* 2019, **211**: 258–263.

[54] Wu YF, Suo H, Zhao XQ, *et al*. Self-calibrated optical thermometer $LuNbO_4$:Pr^{3+}/Tb^{3+} based on intervalence charge transfer transitions. *Inorg Chem Front* 2018, **5**: 2456–2461.

[55] Dang PP, Liu DJ, Yun XH, *et al*. Ultra-broadband cyan-to-orange emitting $Ba_{1+x}Sr_{1-x}Ga_4O_8$:Bi^{3+} phosphors: Luminescence control and optical temperature sensing. *J Mater Chem C* 2020, **8**: 1598–1607.

[56] Liu DJ, Yun XH, Dang PP, *et al*. Yellow/orange-emitting $ABZn_2Ga_2O_7$:Bi^{3+} (A = Ca, Sr; B = Ba, Sr) phosphors: Optical temperature sensing and white light-emitting diode applications. *Chem Mater* 2020, **32**: 3065–3077.

[57] Li C, Li Y, Pun EYB, *et al*. A dual-ratiometric optical thermometry based on Sr_2LaF_7:Er^{3+} crystal-implanted pliable fibers. *Dalton Trans* 2022, **51**: 7997–8008.

[58] Luo HY, Li XY, Wang X, *et al*. Highly thermal-sensitive robust $LaTiSbO_6$:Mn^{4+} with a single-band emission and its topological architecture for single/dual-mode optical thermometry. *Chem Eng J* 2020, **384**: 123272.

[59] Cai PQ, Qin L, Chen CL, *et al*. Optical thermometry based on vibration sidebands in Y_2MgTiO_6:Mn^{4+} double perovskite. *Inorg Chem* 2018, **57**: 3073–3081.

[60] Glais E, Đorđević V, Papan J, *et al*. $MgTiO_3$:Mn^{4+} a multi-reading temperature nanoprobe. *RSC Adv* 2018, **8**: 18341–18346.

[61] Yang SH, Lee YC, Hung YC. Thermometry of red nanoflaked $SrAl_{12}O_{19}$:Mn^{4+} synthesized with boric acid flux. *Ceram Int* 2018, **44**: 11665–11673.

[62] Zhang H, Yang H, Li GG, *et al*. Enhancing thermometric performance via improving indicator signal in Bi^{3+}-doped $CaNb_2O_6$:Ln^{3+} (Ln = Eu/Sm/Dy/Tb) phosphors. *Chem Eng J* 2020, **396**: 125251.

[63] Zhang MX, Jia MC, Sheng TQ, *et al*. Multifunctional optical thermometry based on the transition metal ions doped down-conversion Gd_2ZnTiO_6:Bi^{3+},Mn^{4+} phosphors. *J Lumin* 2021, **229**: 117653.